Journal of Materials Chemistry A

ROYAL SOCIETY OF CHEMISTRY

PAPER

View Article Online
View Journal | View Issue

Cite this: J. Mater. Chem. A, 2026, 14, 3591

Electro-upcycling of PET plastic coupled with hydrogen production using the NiCe@NiTe electrocatalyst

Pooja J. Sharma,[a] Sanjay A. Bhakhar,[a] Manish N. Nandpal,[b] Kaushik A. Bhakhar,[c] Samir G. Patel,[b] Parikshit Sahatiya,[d] C. K. Sumesh[a] and Pratik M. Pataniya*[a]

Microplastic reformation in conjunction with the electrochemical hydrogen evolution has merits for producing value-added chemicals and mitigating environmental pollution. This study presents an approach for producing green hydrogen by electro-oxidizing PET micro-plastics in conjunction with alkaline electrolysis, which produces hydrogen gas at the cathode and a valuable chemical, formic acid, at the anode. In this work, a hierarchically structured NiCe@NiTe heterostructure is deposited on nickel foam *via* facile hydrothermal and chemical bath deposition techniques for PET plastic up-cycling at industrial scale current densities. Owing to the interface synergistic effect, an abundance of catalytically active sites, and regulated interfacial charge-transfer, the NiCe@NiTe catalyst exhibits superior HER performance with an overpotential of 243 mV to achieve a 100 mA cm^{-2} current density. *In situ operando* Raman spectroscopy and impedance spectroscopy show the accelerated catalytic oxidation and abundance of *in situ* formed NiOOH sites. It enables the oxidation of ethylene glycol (EG) at 1.38 V *vs.* RHE at 100 mA cm^{-2}, lowering the anodic potential by 250 mV as compared to oxygen evolution. With high selectivity, the NiCe@NiTe catalyst facilitates the conversion of EG to formate with a faradaic efficiency (FE) of 96.5%. Additionally, the FE for hydrogen evolution is more than 93%. The NiCe@NiTe catalyst shows exceptional stability in PET hydrolysate electrolysis (~70 h). Overall, these findings suggest the capability of the NiCe@NiTe catalyst for highly selective and energy-efficient PET upcycling into value-added chemicals and H_2-fuel production at industrial scale current densities.

Received 8th October 2025
Accepted 1st December 2025

DOI: 10.1039/d5ta08195e

rsc.li/materials-a

1 Introduction

Polyethylene terephthalate (PET) plastics, which have a manufacturing capacity of 70 million tons, are widely used in producing food plastic films, beverage bottles, household appliances, and precision instruments due to their high ductility and transparency.[1,2] Furthermore, PET plastic cannot be properly broken down in the natural environment due to its chemical stability.[3] Thus, promoting efficient methods to break down and recycle the increasing amount of waste plastic is essential. Nowadays, there are many different techniques for recycling plastic trash, including mechanical recycling, pyrolysis, land filling, catalytic conversion, and chemical processes.[3–5] Along with chemical breakdown, electrochemical upcycling has attracted increased attention due to its environmentally beneficial qualities, full recovery potential, and capacity to produce value-added products.[6] For example, in alkaline conditions, polyethylene terephthalate (PET) can hydrolyse effectively to produce terephthalic acid (TPA) and ethylene glycol (EG) monomers, which have a lower oxidation potential.[7] Remarkably, electrocatalysis could convert the common EG monomer into high-value formate/formic acid compounds. Therefore, electrocatalysis shows promise as an innovative method for transforming PET hydrolysate into valuable compounds. Additionally, the hydrogen produced at the cathode during water electrolysis is a crucial factor that must be managed to enhance energy efficiency.

Hydrogen is also well known as a sustainable and eco-friendly energy source that can replace conventional fossil fuels and help with the global energy and environmental concerns. A promising method for producing H_2 is electrochemical water splitting, utilizing alkaline electrolyzers and renewable energy sources. Electrochemical water splitting consists of two half reactions: the cathodic hydrogen evolution reaction (HER) and the anodic oxygen evolution reaction (OER). However, a significant barrier is caused by the inherently slow

[a]Department of Physical Sciences, P D Patel Institute of Applied Sciences, Charotar University of Science and Technology, CHARUSAT, Changa, Gujarat, India. E-mail: pm.pataniya9991@gmail.com

[b]Department of Pharmaceutical Chemistry and Analysis, Ramanbhai Patel College of Pharmacy, Charotar University of Science and Technology, CHARUSAT, Changa, Gujarat, India

[c]Gandhinagar Institute of Pharmacy, Gandhinagar University, Gandhinagar, Gujarat-382721, India

[d]Department of Electrical and Electronic Engineering, BITS Pilani Hyderabad, Secunderabad-500078, India

kinetics of the anodic oxygen evolution reaction (OER) because of its 4-electron transfer reaction ($4OH^- \rightarrow O_2 + 2H_2O + 4e^-$, 1.23 V *vs.* the reversible hydrogen electrode (RHE)).[8,9] This greatly hinders widespread use because it not only increases energy waste but also enhances cost since it depends on noble-metal-based electrocatalysts. Therefore, the OER could be replaced using a thermodynamically more advantageous small molecule, such as urea, EG, formaldehyde, or glycerol, to give their respective oxidation reaction as an alternative to the anodic oxygen evolution reaction (OER) mechanism. Notably, the ethylene glycol (EG) oxidation reaction is highly desirable because it produces advantageous and environmentally friendly formate from waste plastic at the anode and effectively forms hydrogen at the cathode. For example, Wang *et al.* created high-performance $PtRh_{0.02}$@Rh nanowire electrocatalysts that enabled the production of high-value biomass products with an ultralow cell voltage of 0.66 V at 10 mA cm^{-2} current density using EG as the anodic feedstock to produce H_2 from seawater.[10] Chen and colleagues used a Pd–$Ni(OH)_2$ electrocatalyst to upcycle PET plastic in an alkaline environment into terephthalate and glycolate. The electrolyte may be further acidified, and high-purity glycolic acid and terephthalic acid (TPA) could be obtained by separation.[11] More research is required to determine the catalytic effectiveness, especially in seawater conditions.

Therefore, it is very necessary and essential to create effective non-noble metal bifunctional electrocatalysts to replace noble metal-based materials for total water splitting and EG oxidation. A significant amount of work was poured into creating sustainable and effective TM-based electrocatalysts, *e.g.*, transition metal-based sulfides,[12] nitrides,[13] phosphides,[14,15] and layered double hydroxides (LDHs).[16,17] The transition metals could be a reasonable alternative to precious metals because of their tunable electronic structure, low costs, and unfilled d-orbitals that can readily lose or gain electrons. Recent studies have concentrated a lot of attention on Ni and Ce-based materials, particularly Ni-based layered double hydroxides, because of their enormous potential for electrocatalytic applications. The Ni sites in the LDH structure provide the active sites with high-valence states, facilitating water electrolysis.[18] For example, Wang and co-authors demonstrated that adding Ce to CoFe LDH can improve its HER performance in alkaline electrolytes by accelerating electron transport and controlling the electronic structure.[19] Jaramillo's group demonstrated how Ce doping can improve OER activities by changing the electrical structure and geometry of host Ni oxide films.[20] In addition, Duan *et al.* synthesized the $CoNi_{0.25}P$ electrocatalyst and achieved EG oxidative conversion to formate with more than 80% faradaic efficiency.[21] Additionally, Gu and colleagues[11] developed Cu-doped Ni-based catalysts and showed outstanding catalytic performance due to the reconstitution of active species during the EGOR process.

In this paper, a heterostructure of LDH and transition metal chalcogenides (NiCe@NiTe) was selected and synthesized by facile hydrothermal and chemical deposition techniques for efficient EG and PET upcycling applications. The lanthanide element cerium has outstanding electronic/ionic conductivity, good oxygen storage capacity, and reversible surface oxygen ion exchange due to the flexible transition between the Ce^{3+} and Ce^{4+}.[22–24] Catalysts based on transition metal chalcogenides have attracted widespread scientific interest because of their excellent catalytic activity and numerous reservoirs. Notably, the transition metal tellurides are metallic in nature and have superior electronic transport capabilities, electrical conductivity, and mass transfer rates.[25–27] The NiCe@NiTe catalyst exhibited excellent electrocatalytic oxidation reaction in 1.0 M KOH solution, requiring only 1.63 V *vs.* RHE to achieve 100 mA cm^{-2}. Remarkably, this potential was further reduced to 1.46 and 1.38 V *vs.* RHE with the introduction of PET hydrolysate and 0.3 M EG solution, respectively. The as-prepared catalysts demonstrated excellent bifunctional stability over 100 h in 1.0 M KOH, along with superior activity in water electrolysis, requiring a low cell voltage of 1.99 V at 100 mA cm^{-2}, which decreased to 1.70 V and 1.76 V upon the addition of PET and EG, respectively. Furthermore, NiCe@NiTe achieved high faradaic efficiencies for the simultaneous generation of H_2 (>93%) and value-added formate (~96%) at optimal cell voltage. This noble electrocatalytic coupling strategy not only enables the production of high-value chemicals but also addresses plastic waste while promoting energy-efficient hydrogen generation.

2 Experimental section

2.1 Fabrication of the NiCe electrode

Firstly, the 3 × 3 cm nickel foam (NF) was sonicated for 10 minutes in a 2.5 M HCl solution to eliminate surface impurities and oxide layers. The treated electrode was then washed using distilled water and acetone. The cleaned NF was then dried in ambient air. Thereafter, it was immersed in a precursor solution (40 mL) containing $Ce(NO_3)_3 \cdot 6H_2O$ (2 mM), $Ni(NO_3)_2 \cdot 6H_2O$ (4 mM), NH_4F (4 mM), and $CO(NH_2)_2$ (4 mM) under constant stirring (Scheme 1). This precursor solution and NF were transferred into a stainless-steel-lined Teflon autoclave. The autoclave was maintained at 120 °C for 12 h. The prepared electrode was then cleaned using deionized water (DI) and acetone, and then dried in a vacuum oven at 70 °C. This sample was denoted as NiCe.

2.2 Fabrication of the NiTe and NiCe@NiTe electrodes

For the fabrication of NiTe on NF, the chemical bath deposition technique was used. In 35 mL of DI water, 1 mM of $Ni(NO_3)_2 \cdot 6H_2O$, 1 mM of TeO_2, and 0.5 g CTAB were mixed under continuous stirring for 15 min to obtain a homogeneous solution, and then 10 mL of hydrazine hydrate was added as a reducing agent. After that, the pre-treated NF was inserted into the reaction solution and kept at room temperature for 24 hours. Subsequently, the obtained samples were washed with DI water and acetone and then dried in an oven at 70 °C. This sample was denoted as the NiTe electrode. The same process was used to prepare the NiTe@NiCe electrode, but instead of pre-treated NF, the NiCe electrode was utilized. The loading of the catalyst was 1.20 mg cm^{-2} for NiCe, 0.93 mg cm^{-2} for NiTe, and 1.22 mg cm^{-2} for NiCe@NiTe.

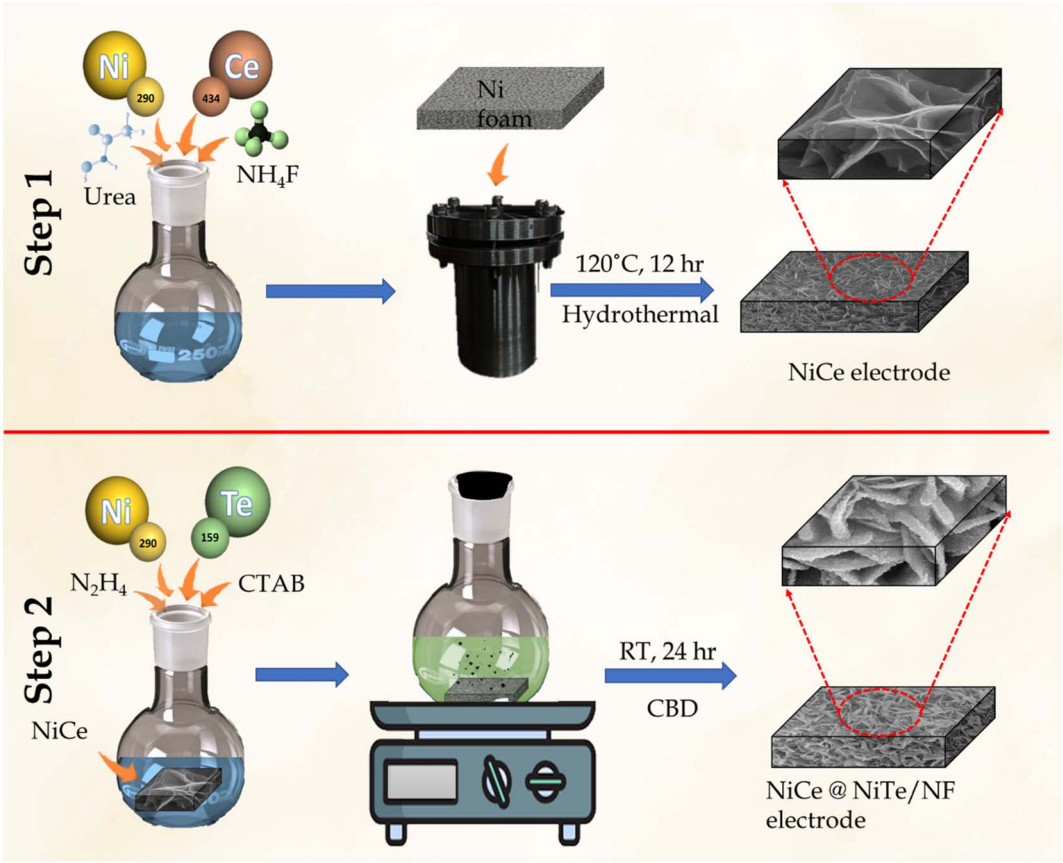

Scheme 1 Synthesis process of the NiCe@NiTe catalysts.

2.3 PET hydrolysate treatment

In order to prepare the PET hydrolysate as the electrolyte, the waste plastic had to be treated. Firstly, the water bottle (4 g) was washed with detergent to remove the dust particles or labels, *etc.*, and then cut into small pieces (1 × 1 cm^2) and added to 50 mL of DI water with 2.0 M KOH. Following that, the mixture containing PET pieces was heated for 15 hours at 160 °C. Subsequently, the resulting PET hydrolysate was diluted with 1.0 M KOH.

2.4 Material characterization

The structural characteristics and phase purity of the as-synthesized electrodes were investigated using a powder X-ray diffractometer (XRD) (Make: Bruker, D2-Phasor, Cu(Kα)). A Field Emission Scanning Electron Microscope (FESEM) equipped with an EDS (Thermo Scientific, Phenom Pharos G2) was used to check the surface morphology and elemental mapping of the prepared samples. The surface chemical composition and chemical states of the prepared electrodes were further investigated using X-ray photoelectron spectroscopy (Thermo Scientific K-alpha XPS).

2.5 Electrochemical analysis

The electrocatalytic properties of the synthesized catalysts were evaluated using the electrochemical workstation PGSTAT-M204 (Make: Metrohm). In the electrochemical measurements, the synthesized catalyst functioned as the working electrode, while Ag/AgCl and a platinum (Pt) wire served as the reference and counter electrodes, respectively. The electrocatalytic performance of the prepared catalysts was examined in different electrolyte environments: 1.0 M KOH, PET hydrolysate, and 1.0 M KOH + 0.3 M EG. Polarization curves were recorded at a scan rate of 5 mV s^{-1}. The measured voltages *vs.* Ag/AgCl were converted into the E_{RHE} using the Nernst formula (1):

$$E_{RHE} = E_{Ag/AgCl} + 0.1976 + (0.059 \times pH) \quad (1)$$

Electrochemical impedance spectroscopy (EIS) was conducted using a sinusoidal wave with an amplitude of 10 mV and a frequency range of 0.01 Hz to 100 kHz. Additionally, cyclic voltammetry was performed in a non-faradaic range with scan rates ranging from 10 to 100 mV s^{-1}.

3 Results and discussion

3.1 Morphological and structural properties of the catalysts

The self-supported NiCe@NiTe catalyst has been synthesized on nickel foam by using a two-step process involving the hydrothermal and chemical bath deposition techniques. The structural phases of the NiCe, NiTe, and NiCe@NiTe catalysts were studied using powder XRD (Fig. 1a). The XRD pattern of

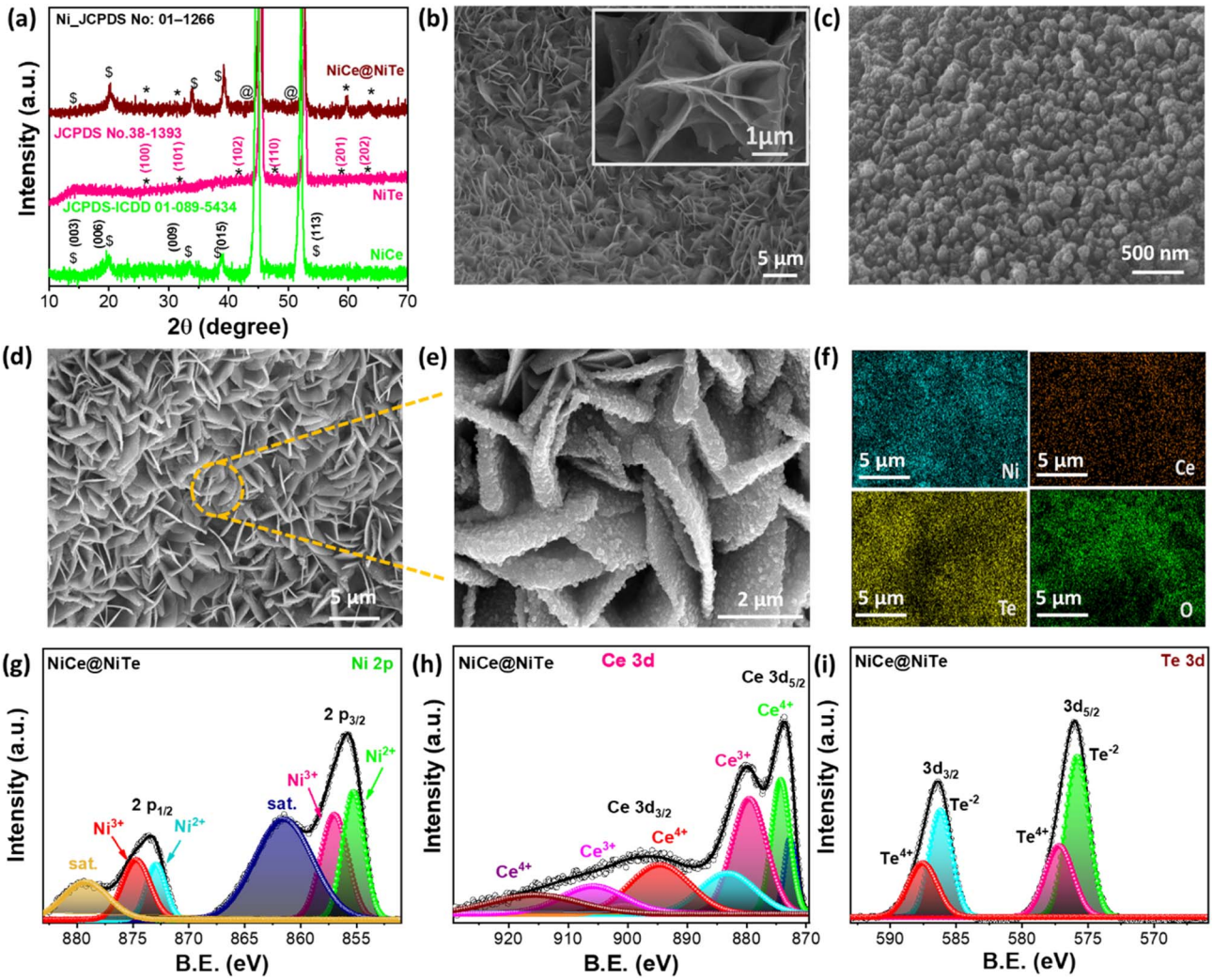

Fig. 1 (a) Powder XRD patterns of the NiCe, NiTe, and NiCe@NiTe catalysts. FESEM images of the (b) NiCe, (c) NiTe, and (d, e) NiCe@NiTe electrodes. (f) EDS elemental maps. (g) The high-resolution XPS spectra of Ni 2p, (h) Ce 3d, and (i) Te 3d.

NiCe exhibited peaks at $2\theta = 12.4°$, 19.87°, 33.39°, 38.90°, and 60.2°, corresponding to the (003), (006), (009), (015), and (113) planes, respectively (JCPDS-ICDD 01-089-5434).[28,29] The XRD pattern of NiTe showed peaks at 31.35°, 41.84°, 47.03°, 58.03°, and 63.78°, corresponding to (101), (102), (110), (201), and (202) crystalline planes, respectively, attributed to the hexagonal crystalline structure (lattice constant ($a = 3.93$ Å and $c = 5.37$ Å), and V = 71.9 Å^3) of NiTe (JCPDS: 38-1393).[30,31] The XRD pattern of NiCe@NiTe confirmed the co-existence of both NiCe and NiTe phases. Additionally, the XRD patterns of the electrodes exhibited prominent peaks at $2\theta = 44.5°$ and 51.9°, attributed to the underlying nickel substrate of the nickel foam (JCPDS no. 01-1266).[32,33]

The FE-SEM analysis with EDS-elemental mapping was employed for the analysis of morphological evolution in the NiCe, NiTe, and NiCe@NiTe electrodes. Fig. 1b shows the FE-SEM images of the NiCe-LDH, displaying the close packing of vertically oriented ultrathin nanosheets. The hierarchical structure of vertical nanosheets with relatively flat terraces is shown in the inset image (Fig. 1b), which is beneficial for enhanced charge and mass transport due to deep diffusion characteristics.[34] In Fig. 1c, the SEM image of the NiTe shows a small cluster of nanoparticles. Importantly, the SEM images of NiCe@NiTe confirmed the decoration of NiTe nanoparticles on NiCe nanosheets, forming the core-shell-type structure (Fig. 1d and e). The NiCe@NiTe array with rough terrace combines the advantages of the hierarchical structure of vertical nanosheets and highly defective nanoparticle arrays, suggesting the abundance of catalytically active sites, and improved electrolyte diffusion and charge transport.[35,36] The FESEM-EDS elemental mapping of the catalysts is displayed in Fig. 1f, confirming the distribution of Ni, Ce, Te, and O in the structure.

The surface chemical composition and valence state of the NiCe@NiTe were analyzed using X-ray photoelectron spectroscopy. The XPS survey spectra (Fig. S1, SI) show the presence of Ni 2p, Ce 3d, Te 3d, and O 1s peaks, indicating the successful synthesis of the NiCe@NiTe. The high-resolution Ni 2p spectra of NiCe@NiTe LDH (Fig. 1g) show two prominent peaks,

deconvoluted into the spin–orbit doublet of Ni $2p_{3/2}$ and Ni $2p_{1/2}$ at 855.39 eV and 873.10 eV, corresponding to Ni^{2+}-sites. Additional peaks at 857.07 eV and 874.79 eV are attributed to the presence of Ni^{3+}-sites, and the remaining two peaks are the satellite peaks. The high-resolution Ce 3d XPS spectra (Fig. 1h) display Ce $3d_{5/2}$ peaks at 872.9, 874.5, 879.9, and 883.5 eV, while Ce $3d_{3/2}$ peaks appeared at 894.6 eV, 900.05 eV, 906.06 eV, and 915.70 eV.[37–40] These confirm the co-existence of Ce^{3+} and Ce^{4+} species in the NiCe@NiTe catalyst, which enhances the electronic transmission capabilities and promotes electrocatalytic activity.[37,38] Fig. 1i presents the high-resolution Te 3d spectra, with peaks at 575.9 eV and 586.22 eV corresponding to Te $3d_{5/2}$ and Te $3d_{3/2}$, respectively, of the Te^{2-} electronic state, while additional peaks at 577.26 eV and 587.64 eV result from oxidized tellurium species.[41] The high-resolution O 1s spectra (Fig. S2a, SI) reveal three distinct peaks at binding energies of 530.1, 531.5, and 532.8 eV. These peaks are ascribed to the O atom in M–O bonding, the O species of hydroxide ions (M–O–H), and structural or adsorbed water molecules (H–O–H), respectively.[33,40] The Raman spectra were further recorded for structural analysis. The Raman spectrum of the NiCe electrode shows the peak at 452 cm^{-1}, confirming the hydroxide phase of the catalysts (Fig. S2a, SI).[28] The peak at 121 cm^{-1} confirms the NiTe-type phase of the catalyst.[42] The Raman spectrum of NiCe@NiTe contains peaks corresponding to the NiCe as well as NiTe phases. Additionally, TEM images were recorded to observe the morphology and to study the structure of NiCe@NiTe (Fig. S2c and d, SI). The HR-TEM images show the lattice fringes corresponding to both NiCe-LDH and NiTe phases, exhibiting interplanar spacings of 0.26 nm indexed to the (009) plane, and 0.22 nm indexed to the (102) plane, respectively.

3.2 Electrocatalytic HER, OER, and EGOR activity

Given the optimized electronic structure and morphological evolution, we have analyzed the electrocatalytic HER and OER performance of the NiCe, NiTe, and NiCe@NiTe self-supported catalysts, commercial Pt/C, RuO_2, and bare NF in alkaline electrolyte (1 M KOH). Fig. 2a shows the iR-compensated

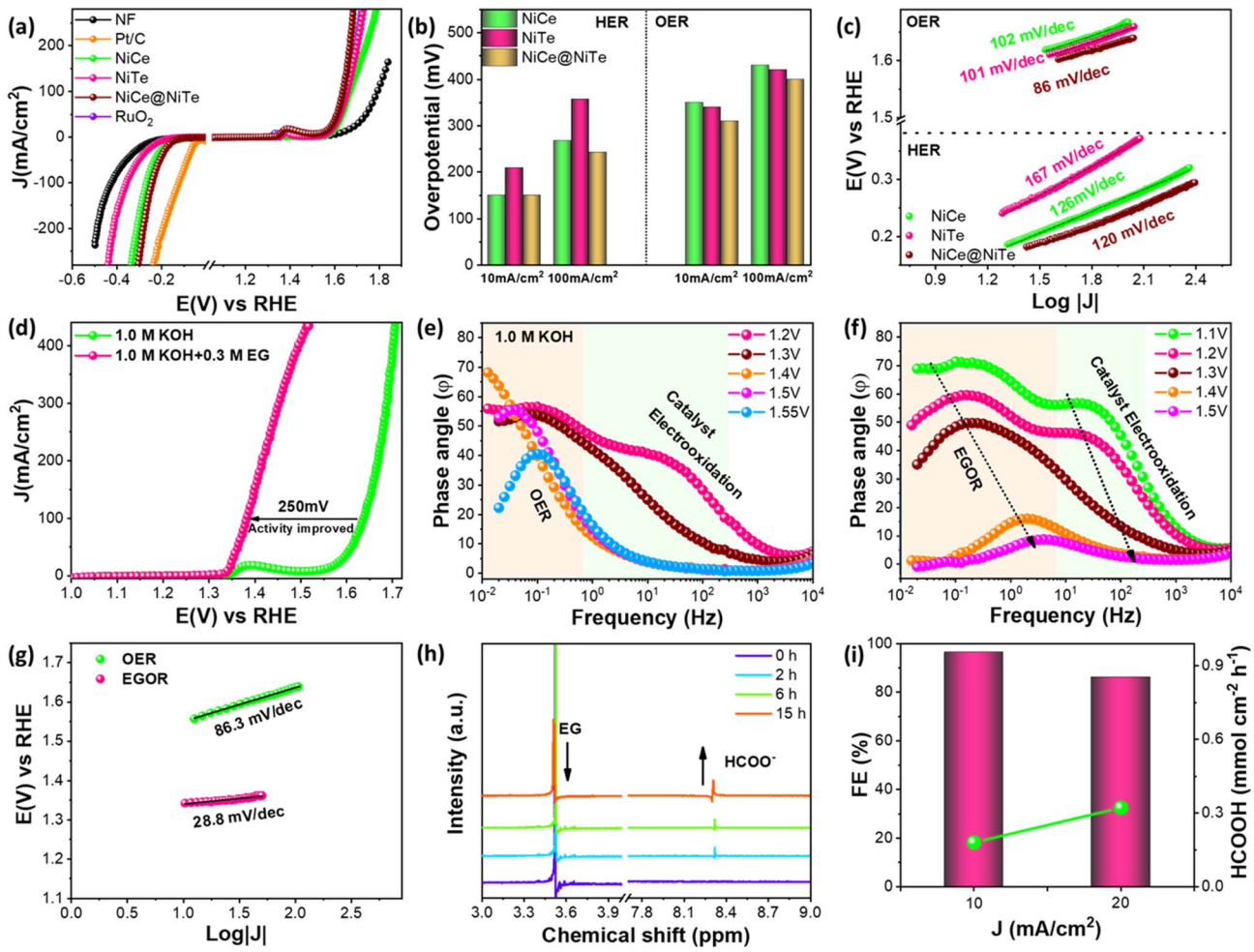

Fig. 2 (a) Linear polarization curves of the as-prepared catalysts in a 1.0 M KOH solution. (b) Overpotential comparison plots at 10 and 100 mA cm^{-2}. (c) Tafel slopes and (d) LSV curves of the NiCe@NiTe catalysts in 1.0 M KOH and 1.0 M KOH + 0.3 M EG solutions. (e) and (f) Bode and phase plots of the NiCe@NiTe catalysts at different potentials. (g) Tafel slopes and (h) ^1H NMR spectra of the EGOR products. (i) Faradaic efficiency and formate yield at different current densities.

polarization curves for the HER and OER activities of all the catalysts. Encouragingly, the NiCe@NiTe catalyst demonstrated superior HER and OER performances as compared to the pristine NiCe and NiTe catalysts, requiring a potential of −0.243 V *vs.* RHE and 1.63 V *vs.* RHE to generate a geometric current density of 100 mA cm^{-2} for the HER and OER, respectively; the pristine NiCe (−0.268 V, 1.86 V *vs.* RHE) and NiTe (−0.357 V, 1.65 V *vs.* RHE) gave inferior catalytic performances. Although the NiCe@NiTe catalyst demonstrated superior OER performance as compared to a commercial catalyst (RuO_2), its HER performance is inferior to that of Pt/C. Additionally, the polarization curves for the OER exhibited the oxidation peak at 1.34 V *vs.* RHE, which is attributed to the oxidation of Ni^{2+} to Ni^{3+} due to the formation of NiOOH species.[34,43] NiCe@NiTe exhibited a slightly intense peak as compared to pristine catalysts, indicating the accelerated oxidation of Ni^{2+}.[34,43] The overpotentials required to achieve the geometric current densities of 10 and 100 mA cm^{-2} for NiCe, NiTe, and NiCe@NiTe catalysts are shown in Fig. 2b. Interestingly, the NiCe@NiTe exhibited superior HER and OER performance in alkaline conditions as compared to previous reports on state-of-the-art non-noble catalysts (Table S2 and S3, SI). To further understand the HER and OER kinetics and pathways of the catalysts in an alkaline medium, a Tafel slope analysis was performed. As shown in Fig. 2c, the Tafel slope values for NiCe@NiTe were found to be 120 mV dec^{-1} and 86 mV dec^{-1} for the HER and OER, respectively, which are smaller than those of the NiCe and NiTe catalysts. This suggests faster charge-transfer kinetics for the HER and OER as compared to pristine catalysts.

The possible proposed HER (eqn (2)–(4)) and OER (eqn (5)–(9)) mechanisms on the surface of the NiCe@NiTe catalysts in an alkaline medium are as follows:[44–47]

HER:

$$M + H_2O + e^- \rightarrow M - H^* + OH^- \text{ (Volmer reaction)} \quad (2)$$

$$M\text{–}H^* + H_2O + e^- \rightarrow M + OH^- + H_2 \text{ (Heyrovsky reaction)} \quad (3)$$

or

$$2M - H^* \rightarrow 2M + 2H_2 \text{ (Tafel reaction)} \quad (4)$$

OER:

$$M + OH^- \rightarrow M\text{–}OH + e^- \quad (5)$$

$$M\text{–}OH + OH^- \rightarrow M\text{–}O + H_2O + e^- \quad (6)$$

$$M\text{–}O + OH^- \rightarrow M\text{–}OOH + e^- \quad (7)$$

$$M\text{–}OOH + OH^- \rightarrow M\text{–}O_2 + H_2O + e^- \quad (8)$$

$$M\text{–}O_2 \rightarrow M + O_2 \quad (9)$$

(*M – surface active sites of the NiCe@NiTe catalyst).

The charge-transfer mechanisms for the HER and OER activities were further analyzed using electrochemical impedance spectroscopy (EIS). As shown in Fig. S3a and b (SI), the NiCe@NiTe catalysts exhibited lower values of charge-transfer resistance as compared to pristine catalysts, and also, the semi-circle in the Nyquist plots indicates the regulated interfacial charge-transport due to the formation of a charge-double layer. Fig. S3c (SI) shows that the NiCe-LDH exhibited superior catalytic performance to $Ni(OH)_2$, showing the synergistic improvement of the HER performance in the bi-metallic catalyst. The normalized polarization curve, calculated from specific current density (in A g^{-1}), further confirmed the superior HER catalytic performance of the NiCe@NiTe heterostructures (Fig. S3d, SI). The electrochemically active surface area (ECSA) is a crucial property for the electrocatalysts. The ECSA is directly proportional to the double-layer capacitance (C_{dl}). The C_{dl} values from NiCe, NiTe, and NiCe@NiTe were evaluated from the cyclic-voltammetry curves recorded in the non-faradaic range at different scan rates (10–100 mV s^{-1}) (Fig. S4(a)–(c), SI). As compared to pristine NiCe (0.084 mF cm^{-2}) and NiTe (0.022 mF cm^{-2}) catalysts, NiCe@NiTe (0.196 mF cm^{-2}) exhibits a higher value of C_{dl}, attributed to the greater abundance of catalytically active sites for NiCe@NiTe (Fig. S4(d)).

Motivated by the excellent HER and OER activities, the catalytic performance of the NiCe@NiTe catalyst for the ethylene glycol oxidation reaction (EGOR) was studied in the 1.0 M KOH + 0.3 EG electrolyte. The polarization curves indicate that NiCe@NiTe showed a superior EGOR performance as compared to NiCe and NiTe, and achieved the current density of 100 mA cm^{-2} at 1.38 V *vs.* RHE (Fig. 2d) (Fig. S5(a), SI), lowering the anodic potential by 250 mV, owing to the thermodynamically favorable nature of the EGOR and the abundance of the catalytically active sites in the NiCe@NiTe heterostructure. The onset of the EGOR coincided well with the peaks for the oxidation of Ni^{2+} to Ni^{3+}, suggesting that the *in situ*-formed NiOOH is the primary active site for the EGOR. NiCe@NiTe, with an abundance of *in situ* formed NiOOH sites, facilitates the highly selective EGOR, allowing electro-oxidation at an industrially large current density of 400 mA cm^{-2} at 1.5 V *vs.* RHE. Further, the NiCe@NiTe catalyst exhibited a significantly lower Tafel slope (28.8 mV dec^{-1}) for the EGOR than that for the OER (86.3 mV dec^{-1}), attributed to the favourable thermodynamic and kinetic EGOR performance (Fig. 2g).

EIS was employed to investigate the charge-transfer kinetics and surface interfacial reaction during the OER and EGOR (Fig. S5(b), S6(a and b), SI). The Nyquist plots (Fig. S6(a)) show a vertical line in the potential range of 1.1–1.3 V *vs.* RHE, indicating the high charge-transfer resistance, revealing the low OER activity. Upon increasing the potential to 1.5 V *vs.* RHE, a distinct semicircle corresponding to charge-transfer resistance (R_{ct}) appeared, and its diameter decreased on further increase of potential, signifying the onset of the OER at ~1.5 V *vs.* RHE. In contrast, the EGOR process exhibited a notable decline in R_{ct} at a lower potential range (1.3 V *vs.* RHE), demonstrating significantly low onset potential (Fig. S6(b), SI). Bode plots were further analyzed to assess phase-angle variations with frequency at different potentials in 1.0 M KOH with and without EG (Fig. 2e and f). The plots can be divided into high- and low-frequency regions, corresponding to the electron conduction in the inner layer of the catalyst and the interfacial

reaction charge-transfer, respectively.[48] In the high-frequency range (~100 Hz), the NiCe@NiTe heterostructure displayed an additional peak at 1.1 V *vs.* RHE, attributed to electro-oxidation of the metal in the catalyst.[49] This peak shifted to higher frequencies with decreased phase angles on increasing potential, attributed to the accelerated charge-transfer in the inner layer of the catalyst (Fig. 2e). The phase angle in the lower frequency region decreased with an increase in potential, showing the efficient charge transfer between OH^- and the catalyst surface.[50] At a potential of 1.5 V *vs.* RHE, the Bode plot exhibited the emergence of a new peak in the lower frequency region due to the onset of the OER. A similar OH* adsorption peak in the lower frequency range and a metal oxidation peak in the higher frequency range were observed during the EGOR in the potential range 1.1–1.2 V *vs.* RHE (Fig. 2f). At 1.3 V *vs.* RHE, a new peak emerged in the EGOR, shifting markedly to lower phase angles with increasing potential, suggesting rapid EGOR initiation on NiCe@NiTe.[50] The EGOR peak is well matched with the metal oxidation peak in 1 M KOH. Furthermore, in the higher frequency region (10 to 10^5 Hz), the heterostructure exhibited lower phase angles at 1.1–1.5 V for both the OER and EGOR, indicating efficient electron conduction through the metallic phase of the catalyst. Meanwhile, in the low-frequency region (10^{-2} to 10^{-1} Hz), the phase angle decreased more rapidly during the EGOR than OER as the potential increased, reflecting enhanced charge transfer and faster kinetics. Collectively, these results confirm that the NiCe@NiTe heterostructure possesses strong adsorption capacity for both OH^- and EG molecules, thereby enhancing catalytic activity and enabling EGOR at lower potentials.[50]

For the qualitative analysis of the EGOR product, ^{1}H NMR was employed. The ^{1}H NMR spectra of electrolysed samples show the presence of EG at 3.53 ppm, and formate ($HCOO^-$) at 8.30 ppm, attributed to the highly selective production of formate ($HCOO^-$), a valuable chemical, during the EGOR (Fig. 2h). Using HPLC, the faradaic efficiency (FE) for formate production was further evaluated for I conversion efficiency (Fig. S7(a–c), SI). The formate production rate was enhanced from 0.18 mmol h^{-1} cm^{-2} at 10 mA cm^{-2} to 0.69 mmol h^{-1} cm^{-2} at 100 mA cm^{-2} (Table S1). The maximum FE of 96.5% was realised at a current density of 10 mA cm^{-2} (Fig. 2i).

3.3 Electrocatalytic mechanism insight

The two main processes involved in electrochemical alcohol oxidation reactions are indirect and direct oxidation.[51] Publications have indicated that an indirect oxidation process is typically used to achieve the electrochemical oxidation of EG on transition metal-based catalysts.[51–53] To verify this point, cyclic voltammetry was recorded in 1.0 M KOH with and without EG. Fig. 3a shows the characteristic Ni^{2+}/Ni^{3+} redox peak in the electrolyte without EG. Upon adding EG to the electrolyte, the Ni^{2+}/Ni^{3+} redox peak disappeared, and the reverse scan process showed a higher reaction current compared to the forward scan. This suggests that EG may reduce the high-valence nickel species *in situ* to its original state (Ni^{2+}). Chronoamperometry was performed at different potentials (Fig. 3b) to further confirm the indirect oxidation mechanism. Initially, anodic oxidation of the electrode was performed at 1.4 V *vs.* RHE in 1.0 M KOH to oxidize the Ni^{2+} to a high-valence state. Subsequently, under open-circuit potential (OCP), EG was introduced to allow chemical interaction between EG and Ni^{3+} species. Afterward, a 1.1 V potential was applied, resulting in a noticeable reduction in current in the 1.0 M KOH electrolyte. It was expected that the reduction of nickel species in the high-valence state would lead to a significant reduction in current in the electrolyte without the addition of EG. In contrast, the reduction current density of NiCe@NiTe decreased significantly upon EG injection, supporting the "Electrochemical–Chemical" oxidation pathway, where Ni^{3+} species are first electro-generated and then undergo a spontaneous chemical reaction by EG.[54,55]

To further study the OER and EGOR behaviour, *in situ* Raman spectroscopy was performed on NiCe@NiTe catalysts at different potentials. During the OER process, two Raman peaks (456 and 533 cm^{-1}) appeared at OCP, which were attributed to Ni-hydroxide. As the potential was applied, these peaks became more intense, and the peaks at 475 and 552 cm^{-1} indicate that Ni hydroxide was converted into NiOOH (Fig. 3c). Upon the addition of EG, the Ni hydroxide vibration signals were suppressed (Fig. 3d and S6c). This implies that the quick reduction of Ni^{3+} in NiOOH enables the oxidation of EG, which is well supported by the cyclic voltammetry and chronoamperometry test (Fig. 3a and b) for the indirect oxidation mechanism, indicating that the Ni^{3+} species in NiCe@NiTe catalysts are the active catalytic intermediates for EG oxidation.

Based on the NMR results and previous research,[21,56–58] a potential reaction pathway of the NiCe@NiTe-driven EGOR process is proposed in Fig. 3e. As illustrated, EG is first oxidized to glycolaldehyde, which is subsequently converted into glyoxal and glycolic acid (GA). Formate is then generated through C–C bond cleavage in glyoxal, whereas both formate and carbonate arise from C–C bond cleavage in GA. Notably, nil amounts of GA and carbonate were detected during EG oxidation, indicating that GA serves merely as a minor intermediate in the overall conversion of EG to formate.

3.4 PET oxidation reaction

Following the excellent EGOR performance of the NiCe@NiTe catalysts, we demonstrated the conversion of the EG derived from real-world PET plastic into high-purity formate (FA). The raw material used in this process was PET water bottles (Fig. S8, SI), which were hydrolyzed using alkaline (KOH) catalysis to generate terephthalate (TPA-K) and EG monomers, with the latter undergoing selective electro-oxidation to produce value-added and separable compounds (Fig. 4a). The iR-compensated polarization curves for the electro-oxidation of PET-hydrolysate on the NiCe@NiTe heterostructure demonstrated that the geometric current densities of 10 and 100 mA cm^{-2} were achieved at 1.4 V and 1.46 V *vs.* RHE, respectively (Fig. 4b), which were lowered by 140 mV and 170 mV compared to the potential required for thermodynamically energy-intensive OER (Fig. 4e). It also gives a better performance than the pristine NiCe, NiTe, and most of the previously

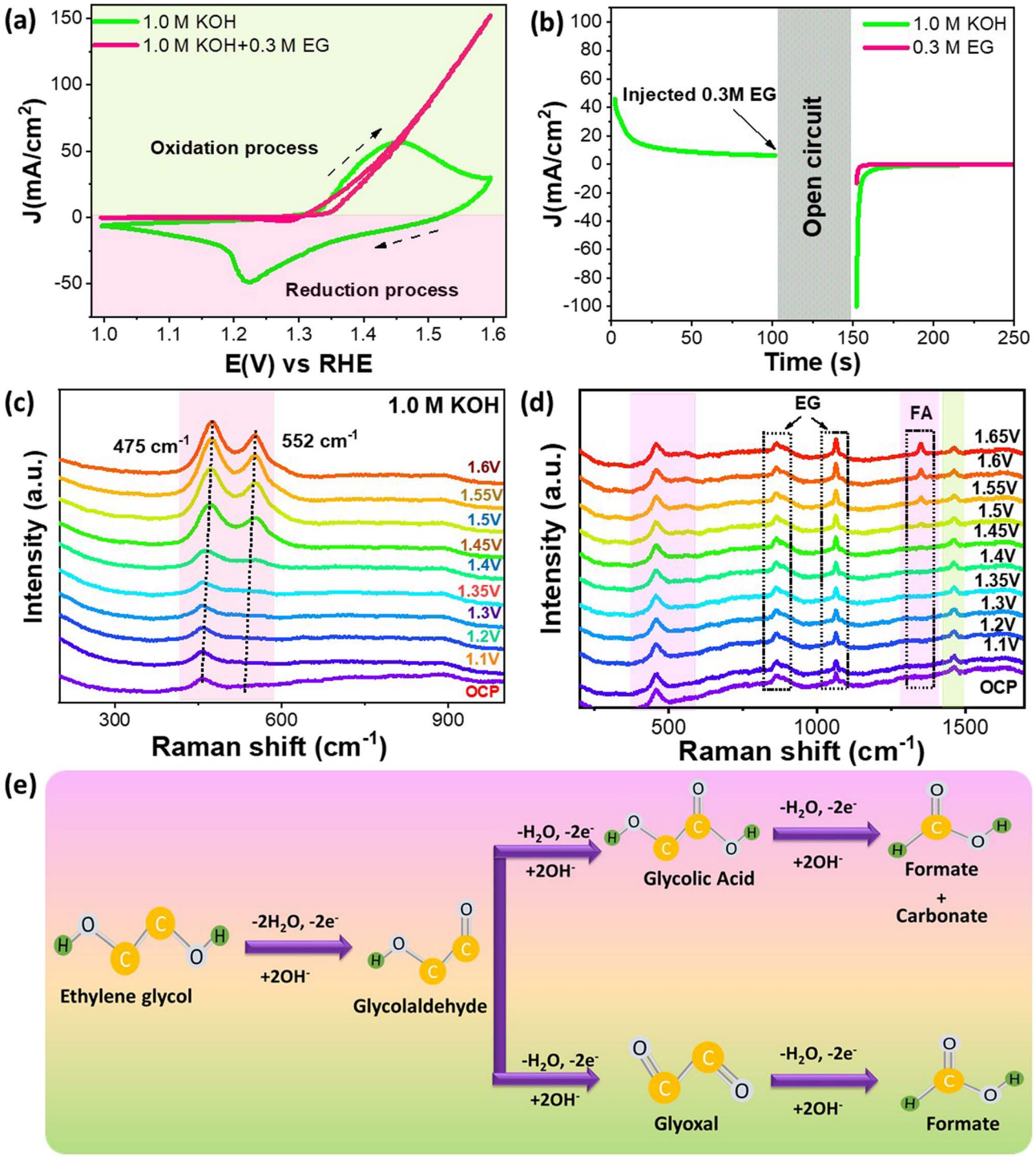

Fig. 3 (a) CV curves, (b) *I*–*t* graph, and (c) and (d) *in situ* Raman spectra of the NiCe@NiTe catalysts for the OER and EGOR. (e) The proposed mechanism of the EGOR on the NiCe@NiTe catalysts.

reported work (Fig. S9(a), Table S4, SI). The energy-efficient oxidation of PET-hydrolysate not only improves the reaction efficiency but also facilitates the production of value-added chemicals, significantly increasing economic viability.

Operando EIS was further performed on NiCe@NiTe catalysts in PET hydrolysate to examine species evolution on the electrode surface and the structure–activity relationship (Fig. S9(b), SI). The low-frequency region (10^{-2} to 10^{1} Hz) corresponds to the non-uniform distribution of charge, which indicates the emergence of oxidized species at the electrode interface, relevant to the catalytic oxidation reaction, while the high-frequency region (10^{1} to 10^{5} Hz) is linked to the internal electrode oxidation.[59] As shown in Fig. 4c, the inflection points of NiCe@NiTe catalysts in the low frequency region occur at 1.4 V

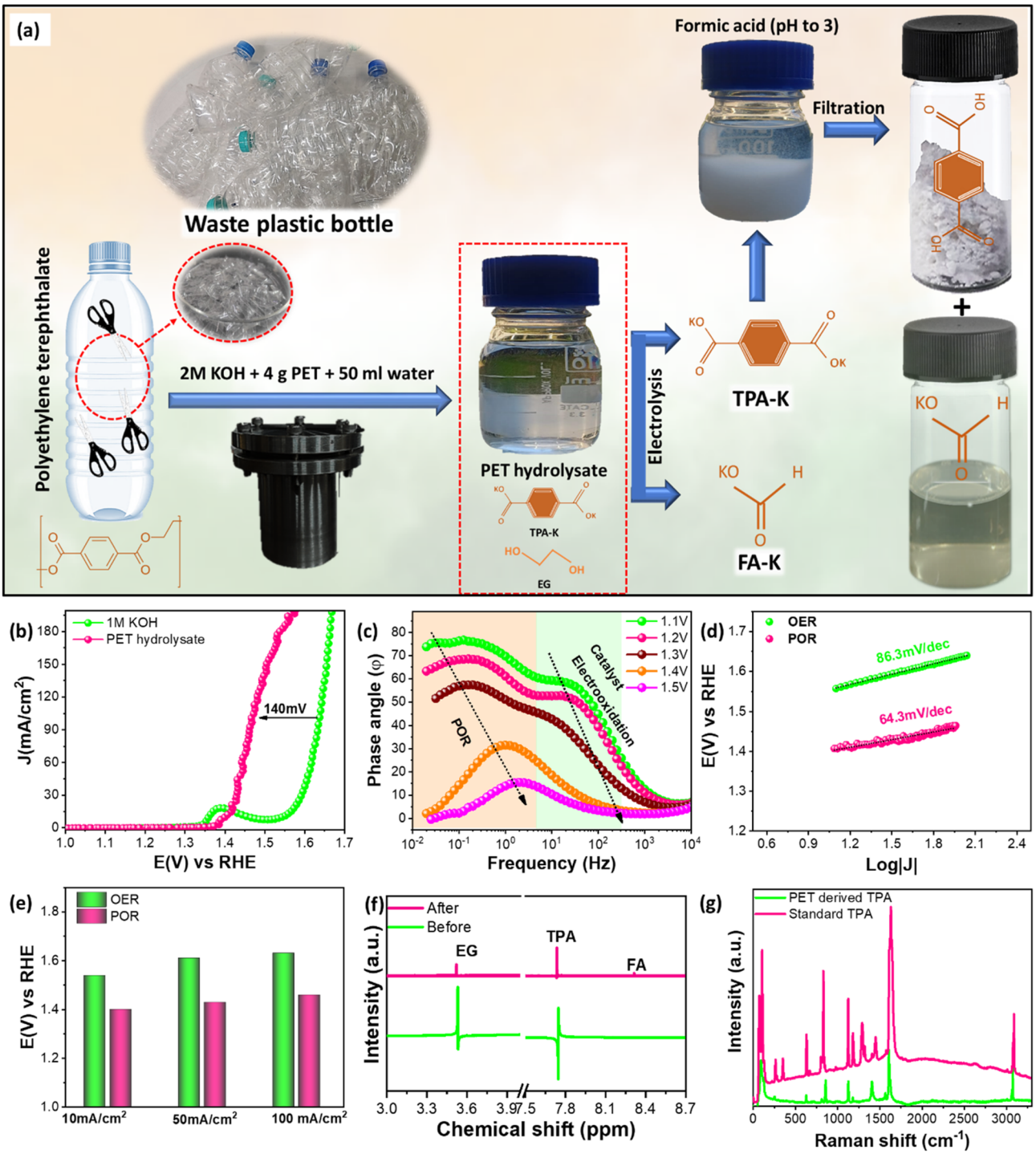

Fig. 4 (a) Schematic of the electrocatalytic water bottle upcycling to TPA and formate. (b) Linear polarization curves of the NiCe@NiTe catalyst with and without PET hydrolysate. (c) Bode plots at different potentials. (d) Tafel plot, (e) overpotential comparison graph at different current densities, (f) ^{1}H NMR spectra of the PET electrolyte, and (g) Raman spectra of the extracted TPA product.

vs. RHE, indicating the onset of the PET oxidation reaction. Notably, compared to the OER, the NiCe@NiTe catalysts in this region exhibit a much smaller phase angle value, suggesting faster reaction kinetics. Subsequently, using a Tafel plot, the electrocatalytic kinetics of the NiCe@NiTe electrode for PET hydrolysate electrooxidation and OER were examined. As shown in Fig. 4d, the Tafel slopes for the OER and POR are 86.3 and 64.3 mV dec^{-1}, respectively, confirming the more favorable catalytic POR kinetics.

For the analysis of the POR product, firstly, the electrooxidation of PET hydrolysate was performed at a current density of 100 mA cm^{-2}. Subsequently, the hydrolysate was

acidified to a pH of ~3 using formic acid, leading to the precipitation of the TPA product. The liquid electrolyte and precipitate were separated by centrifugation at 6000 rpm, and the precipitate was confirmed to be terephthalic acid (TPA, $C_8H_6O_4$) by Raman spectroscopy (Fig. 4g).[60–62] Additionally, the PET hydrolysate was analyzed by ^{1}H NMR spectroscopy. As shown in Fig. 4f, the ^{1}H NMR spectrum of PET hydrolysate displays two peaks at 3.52 ppm and 7.74 ppm corresponding to EG and TPA.[63,64] After electrolysis for 15 h, a new peak appeared at 8.32 ppm, which is attributed to the presence of formate.[65]

3.5 Overall water splitting

Given the superior HER, OER, EGOR, and POR activity of the NiCe@NiTe heterostructure, its effectiveness in promoting energy-efficient hydrogen production was further evaluated through overall water splitting coupled with EG and PET electro-oxidation. The catalytic performance was assessed using three distinct electrolytes, namely 1.0 M KOH, 1.0 M KOH + 0.3 M EG, and PET hydrolysate, by assembling a symmetric electrolyzer in which the prepared catalyst served as both the cathode and anode (Fig. 5a). As shown in Fig. 5d and e, the NiCe@NiTe electrolyzer required only 1.78 V to achieve a current density of 10 mA cm^{-2} in 1.0 M KOH, which was lower than the pristine NiCe, NiTe catalysts, and most of the previously reported work (Fig. S10, Table S5, SI). Notably, the incorporation of 0.3 M EG and PET hydrolysate in 1.0 M KOH solution reduced the required cell voltage to 1.55 V and 1.54 V, respectively. These results demonstrate that PET and EG-assisted electro-oxidation significantly improve energy conversion efficiency for H_2 production compared to conventional water electrolysis.

In addition to its exceptional activity and selectivity, the NiCe@NiTe electrode exhibited excellent stability during water, PET hydrolysate, and EG electrolysis (Fig. 5g, Fig. S11, S12, SI). Across six consecutive cycles, the current density remained

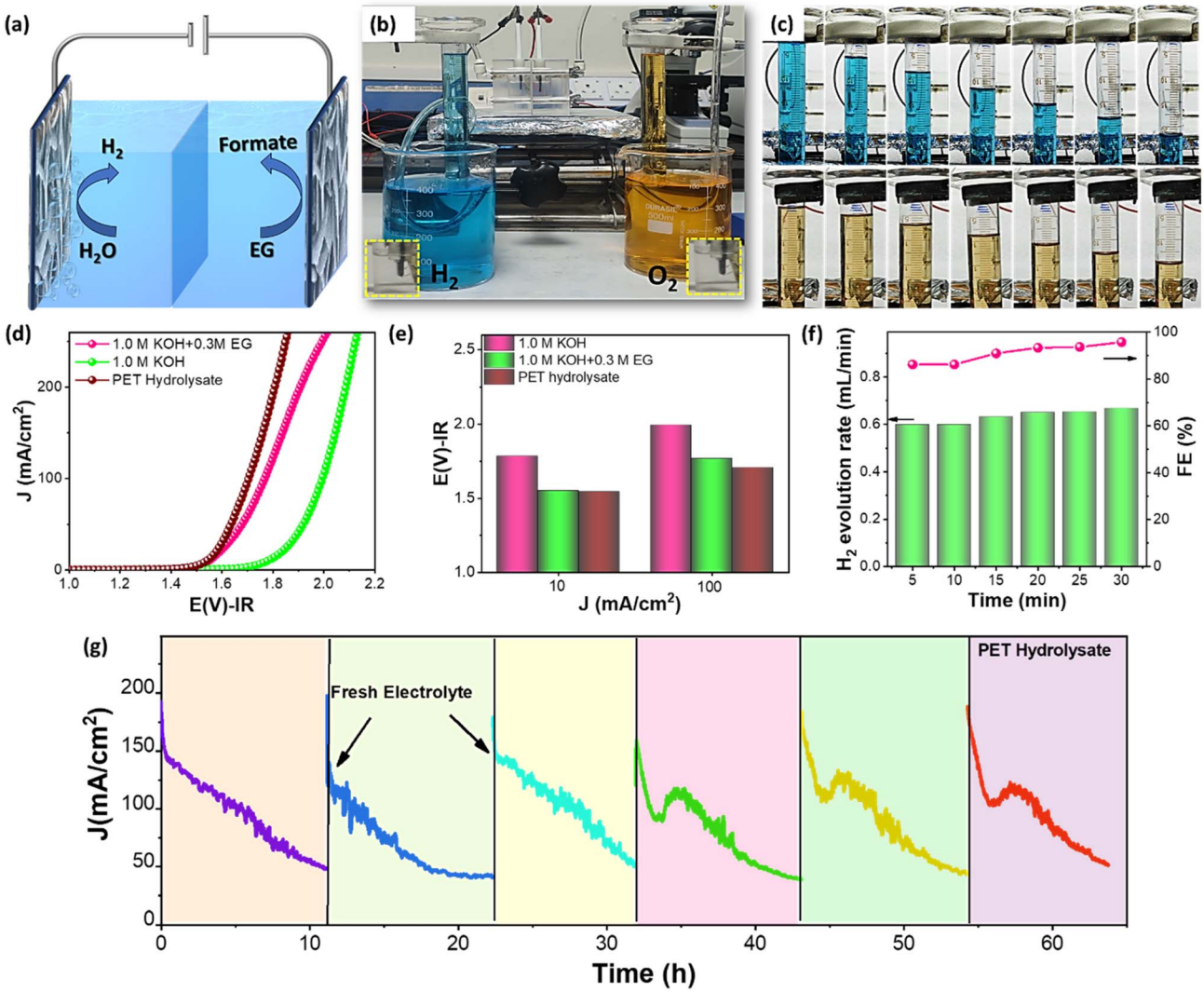

Fig. 5 (a) Schematic of a bifunctional electrolyser. (b) Optical image of the faradaic efficiency measurement device. (c) Optical images of H_2 and O_2 gases collected at different times. (d) LSV curves of the NiCe@NiTe heterostructure in 1.0 M KOH, 1.0 M KOH + 0.3 M EG, and PET hydrolysate. (e) Comparison plot. (f) faradaic efficiency of the H_2 production in a 1.0 M KOH solution. (g) Chrono-potentiometry in the PET hydrolysate.

unchanged, confirming the robustness of the catalyst. As shown in Fig. S11 and S12, a decline in current density was observed during electrolysis, likely due to the depletion of EG in the PET hydrolysate. However, the original current density was restored upon replenishment with fresh electrolyte. To further evaluate long-term durability under industrially relevant conditions, chrono-potentiometry was performed at 100 mA cm^{-2} in the 1.0 M KOH solution. The NiCe@NiTe catalyst exhibited nearly stable performance for over 100 h (Fig. S12, SI), highlighting its excellent durability in continuous water splitting. Post-electrolysis characterization by SEM (inset of Fig. S12, SI) confirmed the retention of the sheet-like morphology, while XRD analysis (Fig. S13, SI) demonstrated that the structural purity of the catalyst was well preserved after extended operation.

The faradaic efficiency of the NiCe@NiTe catalyst was measured using the standard water displacement technique (Fig. 5b and c). The FE values were found to be more than 93% for the HER and OER reactions with yield rates of 1.62 and 0.89 mmol h^{-1}, respectively, indicating the higher conversion efficiency of the NiCe@NiTe catalyst (Fig. 5f, S-14, SI). The electrical energy was further calculated for conventional water electrolysis and PET electrolysis. For the production of 1 Nm^3 of H_2, the electric power consumption for fresh water, EG, and PET-electrolysis were 5.12 kWh Nm^{-3}, 4.55 kWh Nm^{-3}, and 4.40 kWh Nm^{-3}, respectively. Overall, the PET hydrolysate electrolyzer not only enables hydrogen production with lower energy input compared to conventional water electrolysis but also yields valuable products such as formate and TPA. This dual capability underscores the potential of NiCe@NiTe catalysts for sustainable energy conversion and closed-loop recycling of plastic waste.

4 Conclusion

In summary, the NiCe@NiTe nanostructure was successfully synthesized *via* hydrothermal and chemical bath deposition processes. Benefiting from its hierarchical nanostructure and interface synergistic effect, which facilitated electrolyte diffusion and good charge-transfer ability, the NiCe@NiTe catalyst exhibited excellent electrocatalytic activity for industrial-level water electrolysis, as well as EG and PET upcycling. Owing to efficient and superior HER, OER, EGOR and POR performances, the NiCe@NiTe-based electrolyzer requires cell voltages of 1.70 V and 1.76 V to achieve a 100 mA cm^{-2} current density for the electrolysis of PET hydrolysate and EG electrolyte, respectively, which are 290 mV and 230 mV lower than conventional water electrolysis, suggesting the saving of electric energy due to the readily oxidized nature of the EG molecule. The catalyst also demonstrated excellent durability over ~100 h for water electrolysis and ~70 h for PET electrolysis. Additionally, the NiCe@NiTe catalyst exhibited ~93% and ~96.5% FE for H_2 and formate production, respectively. This work presents a unique coordinated approach for the generation of green hydrogen and PET waste plastic upcycling by the use of an economical and effective electrocatalyst.

Conflicts of interest

The authors declare that they have no known competing financial interests or personal relationships that could have appeared to influence the work reported in this paper.

Data availability

Data will be made available on request.

Supplementary information (SI) is available. See DOI: https://doi.org/10.1039/d5ta08195e.

Acknowledgements

The authors are thankful to CHARUSAT for providing the research facilities and financial support to conduct this research. The authors are thankful to the Department of Science & Technology (DST-PURSE) (SR/PURSE/2023/162) for providing the experimental facility for *in situ* Raman spectroscopy and FE-SEM.

References

1 A. Stubbins, K. L. Law, S. E. Muñoz, T. S. Bianchi and L. Zhu, Plastics in the Earth system, *Science*, 2021, **373**, 51–55.
2 M. MacLeod, H. P. H. Arp, M. B. Tekman and A. Jahnke, The global threat from plastic pollution, *Science*, 2021, **373**, 61–65.
3 V. Tournier, C. M. Topham, A. Gilles, B. David, C. Folgoas, E. Moya-Leclair, E. Kamionka, M.-L. Desrousseaux, H. Texier and S. Gavalda, An engineered PET depolymerase to break down and recycle plastic bottles, *Nature*, 2020, **580**, 216–219.
4 H. Zhou, Y. Wang, Y. Ren, Z. Li, X. Kong, M. Shao and H. Duan, Plastic waste valorization by leveraging multidisciplinary catalytic technologies, *ACS Catal.*, 2022, **12**, 9307–9324.
5 Q. Qian and J. Ren, From plastic waste to potential wealth: Upcycling technologies, process synthesis, assessment and optimization, *Sci. Total Environ.*, 2024, **907**, 167897.
6 K. Zheng, Y. Wu, Z. Hu, S. Wang, X. Jiao, J. Zhu, Y. Sun and Y. Xie, Progress and perspective for conversion of plastic wastes into valuable chemicals, *Chem. Soc. Rev.*, 2023, **52**, 8–29.
7 X.-H. Wang, Z.-N. Zhang, Z. Wang, Y. Ding, Q.-G. Zhai, Y.-C. Jiang, S.-N. Li and Y. Chen, Ultra-thin CoNi0.2P nanosheets for plastics and biomass participated hybrid water electrolysis, *Chem. Eng. J.*, 2023, **465**, 142938.
8 J. Du, F. Li and L. Sun, Metal–organic frameworks and their derivatives as electrocatalysts for the oxygen evolution reaction, *Chem. Soc. Rev.*, 2021, **50**, 2663–2695.
9 Z. Yu and L. Liu, Recent Advances in Hybrid Seawater Electrolysis for Hydrogen Production, *Adv. Mater.*, 2024, **36**, 2308647, DOI: 10.1002/adma.202308647.
10 X. Jiang, Z. Dong, Q. Zhang, G.-R. Xu, J. Lai, Z. Li and L. Wang, Decoupled hydrogen evolution from water/seawater splitting by integrating ethylene glycol oxidation

on PtRh 0.02@Rh nanowires with Rh atom modification, *J. Mater. Chem. A*, 2022, **10**, 20571–20579.

11 F. Liu, X. Gao, R. Shi, Z. Guo, E. C. M. Tse and Y. Chen, Concerted and selective electrooxidation of polyethylene-terephthalate-derived alcohol to glycolic acid at an industry-level current density over a Pd− Ni $(OH)_2$ catalyst, *Angew. Chem., Int. Ed.*, 2023, **62**, e202300094.

12 D. Voiry, J. Yang and M. Chhowalla, Recent strategies for improving the catalytic activity of 2D TMD nanosheets toward the hydrogen evolution reaction, *Adv. Mater.*, 2016, **28**, 6197–6206.

13 D. Liu, H. Ai, J. Li, M. Fang, M. Chen, D. Liu, X. Du, P. Zhou, F. Li and K. H. Lo, Surface reconstruction and phase transition on vanadium–cobalt–iron trimetal nitrides to form active oxyhydroxide for enhanced electrocatalytic water oxidation, *Adv. Energy Mater.*, 2020, **10**, 2002464.

14 D. Liu, H. Ai, M. Chen, P. Zhou, B. Li, D. Liu, X. Du, K. H. Lo, K. Ng and S. Wang, Multi-phase heterostructure of CoNiP/CoxP for enhanced hydrogen evolution under alkaline and seawater conditions by promoting H_2O dissociation, *Small*, 2021, **17**, 2007557.

15 Z. Yu, Y. Li, V. Martin-Diaconescu, L. Simonelli, J. Ruiz Esquius, I. Amorim, A. Araujo, L. Meng, J. L. Faria and L. Liu, Highly Efficient and Stable Saline Water Electrolysis Enabled by Self-Supported Nickel-Iron Phosphosulfide Nanotubes With Heterointerfaces and Under-Coordinated Metal Active Sites, *Adv. Funct. Mater.*, 2022, **32**, 2206138, DOI: 10.1002/adfm.202206138.

16 B. Singh, A. K. Patel and A. Indra, Introduction of high valent Mo^{6+} in Prussian blue analog derived Co-layered double hydroxide nanosheets for improved water splitting, *Mater. Today Chem.*, 2022, **25**, 100930.

17 S. Dutta, A. Indra, Y. Feng, T. Song and U. Paik, Self-supported nickel iron layered double hydroxide-nickel selenide electrocatalyst for superior water splitting activity, *ACS Appl. Mater. Interfaces*, 2017, **9**, 33766–33774.

18 J. Zhang, J. Liu, L. Xi, Y. Yu, N. Chen, S. Sun, W. Wang, K. M. Lange and B. Zhang, Single-atom Au/NiFe layered double hydroxide electrocatalyst: probing the origin of activity for oxygen evolution reaction, *J. Am. Chem. Soc.*, 2018, **140**, 3876–3879.

19 S. Liu, J. Zhu, M. Sun, Z. Ma, K. Hu, T. Nakajima, X. Liu, P. Schmuki and L. Wang, Promoting the hydrogen evolution reaction through oxygen vacancies and phase transformation engineering on layered double hydroxide nanosheets, *J. Mater. Chem. A*, 2020, **8**, 2490–2497.

20 J. W. D. Ng, M. García-Melchor, M. Bajdich, P. Chakthranont, C. Kirk, A. Vojvodic and T. F. Jaramillo, Gold-supported cerium-doped NiO_x catalysts for water oxidation, *Nat. Energy*, 2016, **1**, 1–8.

21 H. Zhou, Y. Ren, Z. Li, M. Xu, Y. Wang, R. Ge, X. Kong, L. Zheng and H. Duan, Electrocatalytic upcycling of polyethylene terephthalate to commodity chemicals and H_2 fuel, *Nat. Commun.*, 2021, **12**, 4679, DOI: 10.1038/s41467-021-25048-x.

22 H. S. Jadhav, A. Roy, B. Z. Desalegan and J. G. Seo, An advanced and highly efficient Ce assisted NiFe-LDH electrocatalyst for overall water splitting, *Sustainable Energy Fuels*, 2020, **4**, 312–323.

23 J. Feng, S. Ye, H. Xu, Y. Tong and G. Li, Design and synthesis of $FeOOH/CeO_2$ heterolayered nanotube electrocatalysts for the oxygen evolution reaction, *Adv. Mater.*, 2016, **28**, 4698–4703.

24 F. Liang, Y. Yu, W. Zhou, X. Xu and Z. Zhu, Highly defective CeO_2 as a promoter for efficient and stable water oxidation, *J. Mater. Chem. A*, 2015, **3**, 634–640.

25 L. Yang, H. Xu, H. Liu, D. Cheng and D. Cao, Active site identification and evaluation criteria of *in situ* grown CoTe and NiTe nanoarrays for hydrogen evolution and oxygen evolution reactions, *Small Methods*, 2019, **3**, 1900113.

26 S. Anantharaj, K. Karthick and S. Kundu, $NiTe_2$ nanowire outperforms Pt/C in high-rate hydrogen evolution at extreme pH conditions, *Inorg. Chem.*, 2018, **57**, 3082–3096.

27 B. Tang, J. Zhou, P. Sun, X. Wang, L. Bai, J. Dan, J. Yang, K. Zhou, X. Zhao and S. J. Pennycook, Phase-controlled synthesis of monolayer ternary telluride with a random local displacement of tellurium atoms, *Adv. Mater.*, 2019, **31**, 1900862.

28 N. Askari, M. Tasviri, M. Ghiasi, M. Amiri and M. Wark, One-pot synthesis of NiCe-LDH for efficient electrochemical water splitting: a comprehensive experimental and theoretical study, *Mater. Today Sustain.*, 2024, **26**, 100784.

29 N. Askari, M. Tasviri and D. Taherinia, Rational design of novel NiBi-LDH with enhanced overall water splitting activity, *Int. J. Hydrogen Energy*, 2024, **51**, 869–886.

30 H. T. Zhang, Y. M. Xiong, X. G. Luo, C. H. Wang, S. Y. Li and X. H. Chen, Hydrothermal synthesis and characterization of NiTe alloy nanocrystallites, *J. Cryst. Growth*, 2002, **242**, 259–262.

31 L. Kulandaivel, J. Park, P. Sivakumar and H. Jung, Hydrazine-assisted hydrothermal synthesis of NiTe and $NiTe_2$ nanorods, *J. Mater. Sci.:Mater. Electron.*, 2023, **34**, 1557.

32 W. Liu, J. Bao, M. Guan, Y. Zhao, J. Lian, J. Qiu, L. Xu, Y. Huang, J. Qian and H. Li, Nickel–cobalt-layered double hydroxide nanosheet arrays on Ni foam as a bifunctional electrocatalyst for overall water splitting, *Dalton Trans.*, 2017, **46**, 8372–8376.

33 L. Liu, T. Guan, L. Fang, F. Wu, Y. Lu, H. Luo, X. Song, M. Zhou, B. Hu and D. Wei, Self-supported 3D NiCo-LDH/Gr composite nanosheets array electrode for high-performance supercapacitor, *J. Alloys Compd.*, 2018, **763**, 926–934.

34 P. J. Sharma, K. K. Joshi, S. Siraj, P. Sahatiya, C. K. Sumesh and P. Pataniya, Vanadium-Doped Ni_3S_2: Morphological Evolution for Enhanced Industrial-Scale Water and Urea Electrolysis, *ChemSusChem*, 2024, e202401371, DOI: 10.1002/cssc.202401371.

35 Z. Shi, X. Qi, Z. Zhang, Y. Song, J. Zhang, C. Guo, W. Xu, K. Liu and Z. Zhu, Interface engineering of cobalt-sulfide-selenium core-shell nanostructures as bifunctional electrocatalysts toward overall water splitting, *Nanoscale*, 2021, **13**, 6890–6901, DOI: 10.1039/d1nr00987g.

36 X. Zheng, Y. Cao, X. Han, H. Liu, J. Wang, Z. Zhang, X. Wu, C. Zhong, W. Hu and Y. Deng, Pt embedded Ni_3Se_2@NiOOH

core-shell dendrite-like nanoarrays on nickel as bifunctional electrocatalysts for overall water splitting, *Sci. China Mater.*, 2019, **62**, 1096–1104, DOI: 10.1007/s40843-019-9413-5.

37 H. Duan, T. Wang, X. Wu, Z. Su, J. Zhuang, S. Liu, R. Zhu, C. Chen and H. Pang, CeO_2 quantum dots doped Ni-Co hydroxide nanosheets for ultrahigh energy density asymmetric supercapacitors, *Chin. Chem. Lett.*, 2020, **31**, 2330–2332.

38 G. Liu, M. Wang, Y. Wu, N. Li, F. Zhao, Q. Zhao and J. Li, 3D porous network heterostructure NiCe@NiFe electrocatalyst for efficient oxygen evolution reaction at large current densities, *Appl. Catal., B*, 2020, **260**, 118199.

39 S. Zuo, Y. He, Y. You, X. Shu, M. Wen, Y. Lu, T. Duan, J. Chen, F. Luo and F. Dong, Free occupying mechanism of simulated tetravalent waste ions in $Gd_2Zr_2O_7$ and performance evaluation of the waste forms, *J. Am. Ceram. Soc.*, 2023, **106**, 7088–7097.

40 H. Xu, B. Wang, C. Shan, P. Xi, W. Liu and Y. Tang, Ce-doped NiFe-layered double hydroxide ultrathin nanosheets/nanocarbon hierarchical nanocomposite as an efficient oxygen evolution catalyst, *ACS Appl. Mater. Interfaces*, 2018, **10**, 6336–6345.

41 Z. Wang, P. Guo, M. Liu, C. Guo, H. Liu, S. Wei, J. Zhang and X. Lu, Rational design of metallic $NiTe_x$ ($x = 1$ or 2) as bifunctional electrocatalysts for efficient urea conversion, *ACS Appl. Energy Mater.*, 2019, **2**, 3363–3372.

42 H. Tan, Z. Yu, C. Zhang, F. Lin, S. Ma, H. Huang, H. Li, D. Xiong and L. Liu, Self-supported NiTe@NiMo electrodes enabling efficient sulfion oxidation reaction toward energy-saving and chlorine-free hybrid seawater electrolysis at high current densities, *Energy Environ. Sci.*, 2025, **18**, 1440–1451, DOI: 10.1039/D4EE05379F.

43 P. Tan, Y. Wu, Y. Tan, Y. Xiang, L. Zhou, N. Han, Y. Jiang, S.-J. Bao and X. Zhang, In Situ Fast Construction of Ni_3S_4/FeS Catalysts on 3D Foam Structure Achieving Stable Large-Current-Density Water Oxidation, *Small*, 2023, **20**, 2308371, DOI: 10.1002/smll.202308371.

44 Y. Zheng, Y. Jiao, M. Jaroniec and S. Z. Qiao, Advancing the electrochemistry of the hydrogen-evolution reaction through combining experiment and theory, *Angew. Chem., Int. Ed.*, 2015, **54**, 52–65.

45 B. S. Yeo and A. T. Bell, Enhanced activity of gold-supported cobalt oxide for the electrochemical evolution of oxygen, *J. Am. Chem. Soc.*, 2011, **133**, 5587–5593.

46 L. Chen, H. Zhang, L. Chen, X. Wei, J. Shi and M. He, Facile synthesis of Cu doped cobalt hydroxide (Cu–$Co(OH)_2$) nanosheets for efficient electrocatalytic oxygen evolution, *J. Mater. Chem. A*, 2017, **5**, 22568–22575.

47 J. Feng, H. Xu, Y. Dong, S. Ye, Y. Tong and G. Li, FeOOH/Co/FeOOH hybrid nanotube arrays as high-performance electrocatalysts for the oxygen evolution reaction, *Angew. Chem., Int. Ed.*, 2016, **55**, 3694–3698.

48 Y. Li, X. Liu, K. Wang, J. Chi, H. Lin and L. Wang, Oxygen vacancy assisted Ru–$Ni(OH)_2$ for efficient ethylene glycol electrooxidation reaction, *Inorg. Chem. Front.*, 2024, **11**, 6889–6897.

49 S. Zhong, B. He, S. Wei, R. Wang, R. Zhang and R. Liu, Dynamic Fe-O-Cu induced electronic structure modulation on CuO_x electrode for selective electrocatalytic oxidation of glycerol, *Appl. Catal., B*, 2025, **362**, 124743, DOI: 10.1016/j.apcatb.2024.124743.

50 F. Ma, Z. Li, R. Hu, Z. Wang, J. Wang, J. Li, Y. Nie, Z. Zheng and X. Jiang, Electrocatalytic Waste-Treating-Waste Strategy for Concurrently Upgrading of Polyethylene Terephthalate Plastic and CO_2 into Value-Added Formic Acid, *ACS Catal.*, 2023, **13**, 14163–14172, DOI: 10.1021/acscatal.3c03428.

51 W. Li, D. Xiao, X. Gong, X. Xu, F. Ma, Z. Wang, P. Wang, Y. Liu, Y. Dai, Z. Zheng, Y. Fan and B. Huang, Electrocatalytic upgrading of polyethylene terephthalate plastic to formic acid at an industrial-scale current density *via* Ni-MOF@MnCo-OH catalyst, *Chem. Eng. J.*, 2024, **480**, 148087, DOI: 10.1016/j.cej.2023.148087.

52 H. Kang, D. He, X. Yan, B. Dao, N. B. Williams, G. I. Elliott, D. Streater, J. Nyakuchena, J. Huang, X. Pan, X. Xiao and J. Gu, Cu Promoted the Dynamic Evolution of Ni-Based Catalysts for Polyethylene Terephthalate Plastic Upcycling, *ACS Catal.*, 2024, **14**, 5314, DOI: 10.1021/acscatal.3c05509.

53 X. Huang, Y. Guo, Y. Zou and J. Jiang, Electrochemical oxidation of glycerol to hydroxypyruvic acid on cobalt (oxy) hydroxide by high-valent cobalt redox centers, *Appl. Catal., B*, 2022, **309**, 121247.

54 W. Chen, C. Xie, Y. Wang, Y. Zou, C.-L. Dong, Y.-C. Huang, Z. Xiao, Z. Wei, S. Du and C. Chen, Activity origins and design principles of nickel-based catalysts for nucleophile electrooxidation, *Chem*, 2020, **6**, 2974–2993.

55 P. M. Pataniya, P. J. Sharma, S. A. Bhakhar, M. Patel, M. Nandpal, K. A. Bhakhar, S. Patel, P. Sahatiya, G. Nagaraju and C. K. Sumesh, Binder-free Nickel Iron Selenide Catalyst arrays for coupling hydrogen production with polyethylene terephthalate plastic electro-upcycling, *J. Mater. Chem. A*, 2025, DOI: 10.1039/d5ta06515a.

56 F. Liu, X. Gao, R. Shi, E. C. M. Tse and Y. Chen, A general electrochemical strategy for upcycling polyester plastics into added-value chemicals by a $CuCo_2O_4$ catalyst, *Green Chem.*, 2022, **24**, 6571–6577, DOI: 10.1039/d2gc02049a.

57 B. Zhang, H. Zhang, Y. Pan, J. Shao, X. Wang, Y. Jiang, X. Xu and S. Chu, Photoelectrochemical conversion of plastic waste into high-value chemicals coupling hydrogen production, *Chem. Eng. J.*, 2023, **462**, 142247.

58 J. Wang, X. Li, T. Zhang, Y. Chen, T. Wang and Y. Zhao, Electro-reforming polyethylene terephthalate plastic to co-produce valued chemicals and green hydrogen, *J. Phys. Chem. Lett.*, 2022, **13**, 622–627.

59 Y. Qi, Y. Zhang, L. Yang, Y. Zhao, Y. Zhu, H. Jiang and C. Li, Insights into the activity of nickel boride/nickel heterostructures for efficient methanol electrooxidation, *Nat. Commun.*, 2022, **13**, 4602.

60 Z. Chen, R. Zheng, T. Bao, T. Ma, W. Wei, Y. Shen and B.-J. Ni, Dual-Doped Nickel Sulfide for Electro-Upgrading Polyethylene Terephthalate into Valuable Chemicals and Hydrogen Fuel, *Nano-Micro Lett.*, 2023, **15**, 210, DOI: 10.1007/s40820-023-01181-8.

61 M. W. Lee, M. S. Kim and K. Kim, Infrared and Raman spectroscopic study of terephthalic acid adsorbed on silver surfaces, *J. Mol. Struct.*, 1997, **415**, 93–100, DOI: 10.1016/S0022-2860(97)00081-1.

62 L. Sun, Y. Zhao, Y. Shang, C. Sun and M. Zhou, The phase stability of terephthalic acid under high pressure, *Chem. Phys. Lett.*, 2017, **689**, 56–61.

63 S. Song, J. Zhang, G. Gözaydın and N. Yan, Production of terephthalic acid from corn stover lignin, *Angew. Chem., Int. Ed.*, 2019, **58**, 4934–4937.

64 F. Ma, S. Wang, X. Gong, X. Liu, Z. Wang, P. Wang, Y. Liu, H. Cheng, Y. Dai, Z. Zheng and B. Huang, Highly efficient electrocatalytic hydrogen evolution coupled with upcycling of microplastics in seawater enabled *via* Ni_3N/W_5N_4 janus nanostructures, *Appl. Catal., B*, 2022, **307**, 121198, DOI: 10.1016/j.apcatb.2022.121198.

65 H. Yang, N. Han, J. Deng, J. Wu, Y. Wang, Y. Hu, P. Ding, Y. Li, Y. Li and J. Lu, Selective CO_2 reduction on 2D mesoporous Bi nanosheets, *Adv. Energy Mater.*, 2018, **8**, 1801536.

